Smart Nanosensors for *In-Situ* Temperature Measurement in Fractured Geothermal Reservoirs

Mohammed Alaskar[1], Morgan Ames[1], Chong Liu[2], Steve Connor[2], Roland Horne[1], Kewen Li[1], Yi Cui[2]

askar@stanford.edu; mames@stanford.edu; chong813@stanford.edu; horne@stanford.edu; stconnor@stanford.edu,kewenli@stanford.edu; yicui@stanford.edu

[1]Department of Energy Resources Engineering, Stanford University
367 Panama Street, Stanford, CA 94305-2220, USA
[2]Department of Materials Science and Engineering, Stanford University
496 Lomita Mall, Stanford, CA 94305-4034, USA

Temperature measurements are important for the optimum development and energy extraction of enhanced and conventional geothermal resources. Currently, temperature is only measured in the wellbore, as no technology exists to provide information far into the formation. The development of temperature-sensitive nanotracers could allow for such measurements virtually anywhere in the formation.

This paper describes the synthesis and characterisation of two types of temperature-sensitive particles: tin-bismuth alloy nanoparticles and silica nanoparticles with covalently linked dye. Three experiments were performed with the tin-bismuth nanoparticles: a heating test, a slim-tube injection, and a Berea sandstone core injection. Both the heated sample and the effluent samples were characterised using Scanning Electron Microscopy (SEM) and Dynamic Light Scattering (DLS). A heating experiment was also performed with the dye-linked silica particles, and the heated sample was characterised using SEM imaging and fluorimetry.

The feasibility of using nanomaterials as tracers to measure reservoir temperature in-situ and estimate the geolocation of these measurements is addressed.

Keywords: in-situ temperature measurement, nanoparticles.

1. Introduction

There is currently no practical way to measure the reservoir temperature and pressure beyond the wellbore region. The overall goal of this research is to develop nanomaterials capable of measuring reservoir temperature and pressure and correlating such information to fracture connectivity and geometry. This idea is based on the fact that certain types of nanomaterials have the property of undergoing observable changes as a function of temperature and pressure, and that nanoparticles are of the appropriate size to fit through the reservoir pore spaces. Temperature-sensitive nanotracers could be used to assess reservoir performance by measuring temperature far from the wells, thereby providing thermal breakthrough information. Temperature-sensitive nanomaterials have already been developed and used in the biomedical industry for drug delivery. Thus, synthesising temperature-sensitive nanomaterials for geothermal applications is a feasible goal.

Making functional nanomaterials for reservoir sensing involves novel material syntheses to fabricate them and new reservoir engineering approaches to infer reservoir parameters based on the study of their transport properties. Several pressure- and temperature-sensitive nanoparticle concepts have been explored, but are subject to further evaluation from material and reservoir engineering standpoints. Each candidate chosen for investigation will be evaluated according to the following criteria: mobility in reservoir rock, temperature sensitivity, ease of recovery and detection, accuracy of sensing and ease of corresponding analyses, cost, and toxicity.

In order to accomplish the objectives of this study, syntheses of temperature-sensitive nanoparticles were explored for proof of concept and ultimate development. Preliminary heating experiments were conducted to investigate temperature sensitivity, and flow experiments were conducted to investigate the feasibility of transporting these nanoparticles through porous and fractured rocks. An initial investigation of the feasibility of estimating the geolocation of temperature measurements was also performed. The overall objective was to identify and understand the processes involved in the development and use of tailored nanosensors.

2. Tin-bismuth Alloy Nanoparticles

Tin-bismuth alloy nanoparticles were chosen for our first investigation of temperature-sensitive nanoparticles. This alloy has a melting temperature that is tunable between 139°C and 271°C by adjusting its composition, as shown in the phase diagram in Figure 1. A simple sensing scheme of melting and subsequent particle growth was conceived. The growth of native gold nanoparticles upon melting in geologic Arsenian pyrite has been observed by Reich et al. (2006) using transmission electron microscopy during in situ heating to 650°C. It was shown that when the gold nanopar-

ticles melted, they became unstable, leading to diffusion-driven Ostwald ripening and ultimately resulting in the coarsening of the size distribution. We hypothesised that upon melting, the size distribution of tin-bismuth alloy nanoparticles would also coarsen.

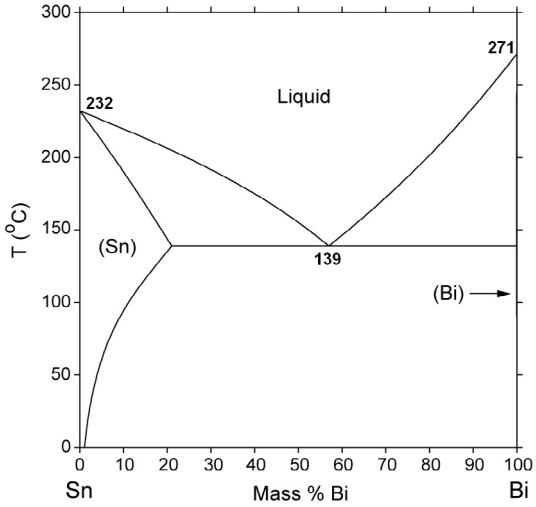

Figure 1: Phase diagram of tin-bismuth (NIST).

Tin-bismuth alloy nanoparticles of eutectic composition were synthesised via ultrasonic processing. These particles were characterised using DLS and SEM imaging. A bench heating experiment was also performed to study the thermal sensitivity of these nanoparticles. The sample was characterised again with DLS and SEM imaging after heating. Injection experiments were performed in a slim-tube packed with glass beads and a Berea sandstone core, and effluent samples were analysed with DLS and SEM imaging.

2.1 Synthesis of tin-bismuth alloy nanoparticles

To perform the synthesis, Sn and Bi were melted together at the eutectic composition (~60 wt % Bi and ~40 wt % Sn). After the alloy was cooled to room temperature, 100 mg was sonicated in 10 ml of mineral oil, a slight variation of the sonochemical method suggested by Chen (2005). The VC-505 ultrasonic processor manufactured by Sonics & Materials, Inc. with a 0.75 in. diameter high gain solid probe was used. The sonicator was operated at 200 W (~95% amplitude) with a pulse setting of 20 s on, 10 s off. The mixture was cooled to room temperature. The alloy particles were washed and centrifuged several times with a 1:1 mixture of hexane and acetone, rinsed in a solution of 0.1 M polyvinyl pyrrolidone (PVP) in ethanol, and finally suspended in ethanol. The centrifuge setting was 6000 rpm for 15 minutes each time.

2.2 Characterisation of tin-bismuth alloy nanoparticles

The tin-bismuth alloy nanoparticles were characterised in terms of size and shape using DLS and SEM imaging.

It was determined from three consecutive DLS measurements that there was a wide distribution of the particle hydrodynamic diameter, as shown in Figure 2.

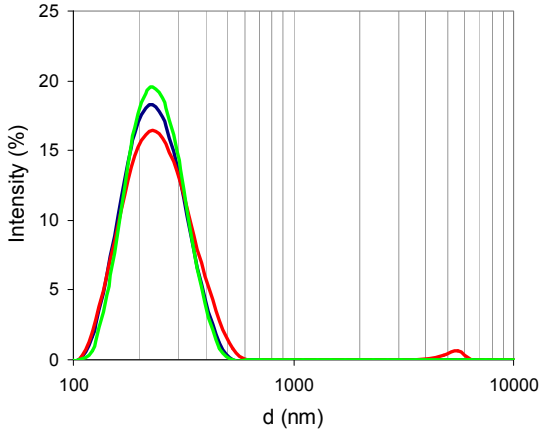

Figure 2: Logarithmic particle size distribution based on hydrodynamic diameter for original tin-bismuth nanoparticle sample.

The three measurements are in reasonable agreement, with an average modal value of 235 nm. The hydrodynamic diameter ranged from ~100 nm to ~600 nm, with Run 2 showing a small peak at ~5500 nm. This indicates that there may have been large particles in the sample, either due to aggregation or from the original synthesis.

The SEM images of the sample show good agreement with the DLS measurements, as shown in Figures 3 – 5.

It is apparent from Figures 3 – 5 that the tin-bismuth nanoparticles range from 50 nm to less than 600 nm. Furthermore, although many of the nanoparticles seem to be spherical as expected, the presence of nonspherical crystalline structures indicates that the sonochemical synthesis did not reach completion. Aggregation on the substrate is observed in both figures, but it is unclear whether this aggregation occurs in solution or upon drying on the substrate. The DLS results suggest that the latter may be the case.

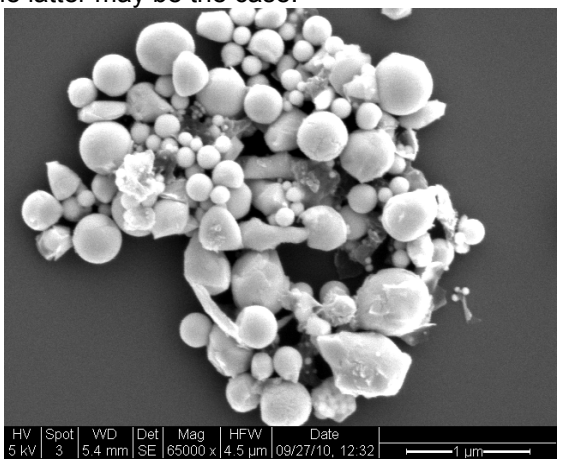

Figure 3: SEM image showing the wide range of tin-bismuth nanoparticle sizes.

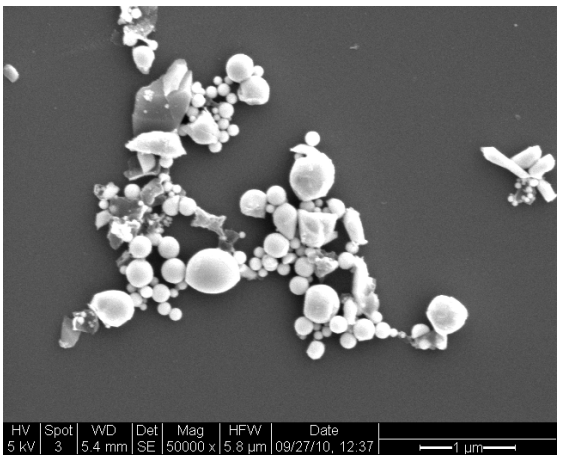

Figure 4: SEM image showing the wide range of tin-bismuth nanoparticle sizes.

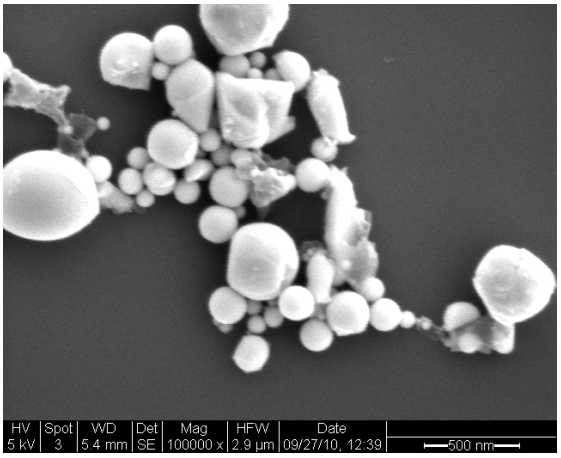

Figure 5: SEM image of tin-bismuth nanoparticles at higher magnification.

2.3 Tin-bismuth nanoparticle heating experiment

To begin investigating the melting behavior of tin-bismuth nanoparticles within the temperature range of interest, a sample of the nanofluid (tin-bismuth in mineral oil) was subjected to a preliminary heating experiment. Although ultimately we are interested in the melting behavior of the tin-bismuth nanoparticles in water, the heating experiments were performed in oil due to the complications associated with the boiling of water at experimental conditions. As shown in the phase diagram Figure 1, at the eutectic composition, the tin-bismuth alloy melts at 139°C. In fact, the nanoparticles likely melt at a slightly lower temperature than this due to melting point depression due to their size.

2.4 Experimental methods used in heating

The sample was heated using a heating mantle connected to a temperature controller with a feedback thermometer, as shown in Figure 6.

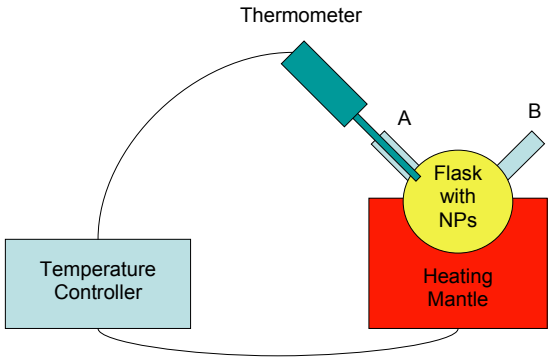

Figure 6: Experimental apparatus for tin-bismuth heating experiment

The flask containing the tin-bismuth nanoparticles in oil was placed in the heating mantle, which was connected to the temperature controller. The temperature controller was also connected to a thermometer, the feedback from which affected whether the mantle was heated, cooled, or maintained and the rate at which this was done. The thermometer was positioned in port A.

The sample was heated in steps to the expected melting point of 139°C. The sample was monitored for a color change near the expected melting point, and when none occurred, the sample was heated in steps to 210°C. No color change ever occurred, but the heating was stopped to prevent the mineral oil from burning. Also, it is likely that melting occurred regardless of the absence of color change. Finally, when the apparatus was at room temperature, the sample was removed from the flask.

The sample was then washed and centrifuged several times with a 1:1 mixture of hexane and acetone, rinsed in a solution of 0.1 M PVP in ethanol, and finally suspended in ethanol. The centrifuge setting was 6000 rpm for 15 minutes each time. This sample was characterised using DLS and SEM imaging.

2.5 Heating experiment results

The DLS results of the sample subjected to heating are shown in Figure 7.

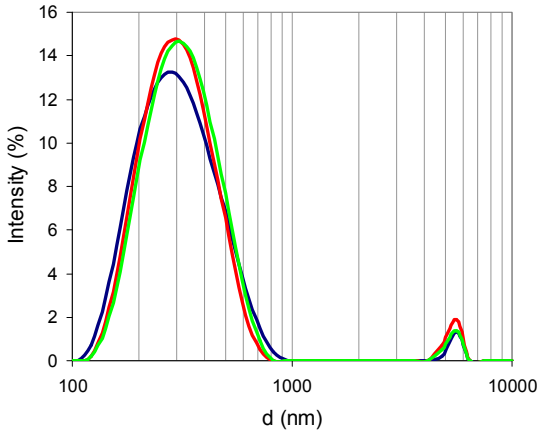

Figure 7: Logarithmic particle size distribution based on hydrodynamic diameter for heated tin-bismuth nanoparticle sample.

The three measurements are in relatively close agreement, with an average modal value of 321 nm. The hydrodynamic diameter ranged from ~100 nm to ~1000 nm. Appreciable secondary peaks in the range of ~4100 nm to ~6400 nm were observed for all runs. This indicates that there are large particles in the sample, most likely due to aggregation and fusion of the particles. Selected particle size distribution curves for comparison of the original and heated samples are shown in Figure 8.

As shown in the figure, the particle size distribution peak shifted noticeably to a larger size. Also, the secondary peak in the micron scale is noticeably larger, indicating that there are more large aggregates. SEM images of the heated sample are shown in Figures 9 and 10.

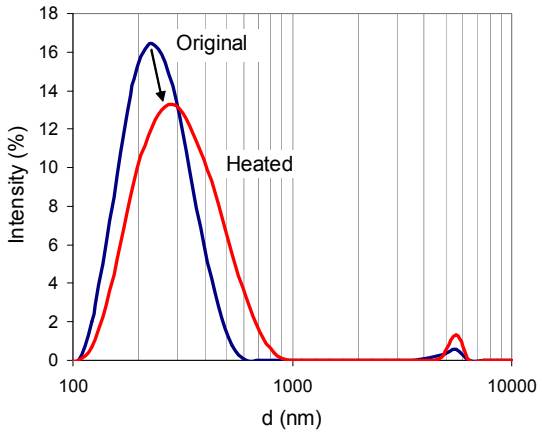

Figure 8: Comparison of logarithmic particle size distribution based on hydrodynamic diameter for original and heated tin-bismuth nanoparticle samples.

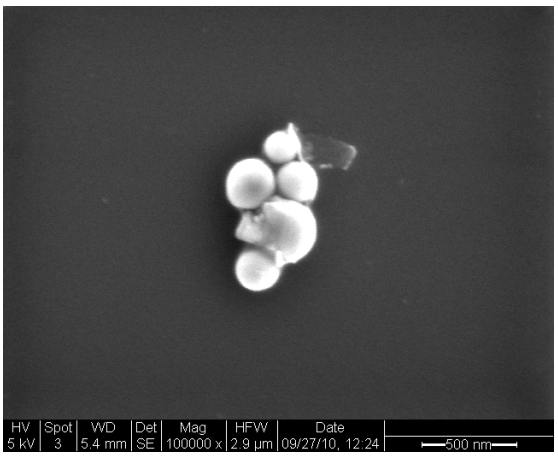

Figure 9: SEM image showing heated tin-bismuth nanoparticles.

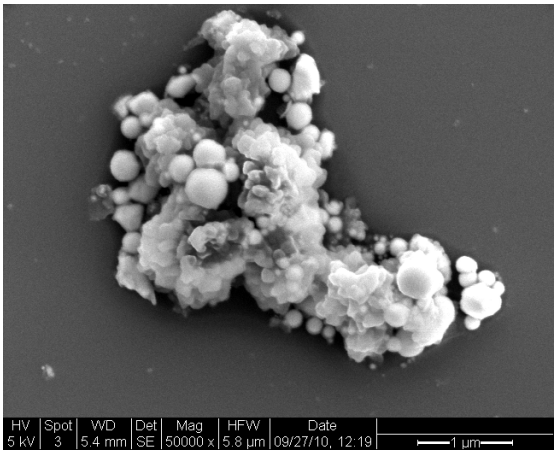

Figure 10: SEM image showing large aggregate of heated tin-bismuth nanoparticles.

Fusion of melted particles can be observed in both figures, and the sizes of both particles and large aggregates are within the range suggested by DLS results. While the fusion of melted particles could account for the shift in particle size distribution, it is difficult to reach any definite conclusions from the SEM results due to the very wide particle size distributions of both the heated and unheated samples. To avoid this ambiguity, the synthesis will be repeated with adjusted parameters in order to achieve a more uniform particle size distribution. Additionally, heating experiments will be repeated directly on a silicon substrate, and a small region of this substrate will be marked for unambiguous SEM analysis.

2.6 Tin-bismuth nanofluid injection experiments

Because of the temperature sensitivity of the tin-bismuth alloy nanoparticles and their potential to be used as a geothermal resource temperature sensor, transport of these particles through porous media was investigated. The nanoparticle suspensions were injected into a slim tube packed with glass beads and into a Berea sandstone core.

2.7 Berea sandstone and slim tube characterisation

The porosity of the core sample was measured by resaturation with pure water and found to be around 17.5% with pore volume in the order of 10 cm^3.

The liquid permeability was measured by introducing pure water at different flow rates ranging from 1 to 5 cm^3/min. The average permeability was found to be approximately 125.4 *md*. By mercury intrusion, it was found that the sandstone core has pore sizes in the range from 0.01 to 20 *μm.*

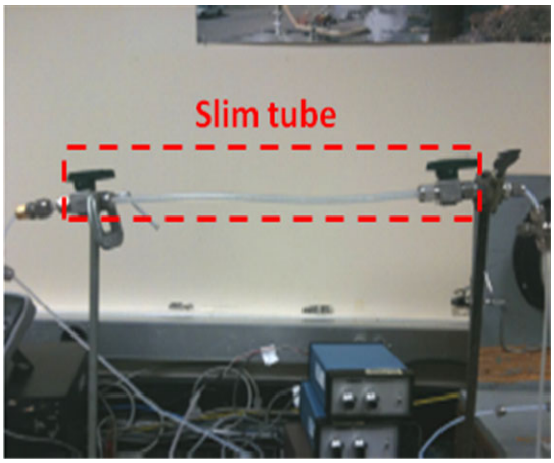

Figure 11: Polypropylene slim tube packed with glass beads.

To investigate the mobility of nanoparticles in the absence of rock materials (such as clays), the nanoparticles were injected into a slim tube packed with glass beads. A 30 *cm* long polypropylene slim tube was constructed. The tube was packed with glass beads (Glasperlen 0.1 *cm* in diameter from B. Braun Biotech International) and fitted with screens and valves at each end. This polypropylene slim tube is pictured in Figure 11. The permeability and pore volume of the slim tube packed with glass beads were found to be approximately 18.1 *md* and 2.6 cm^3, respectively.

2.8 Experimental methods used in injection

Tin-bismuth nanoparticle injections were conducted to investigate their flow mechanism through the pores of Berea sandstone. The apparatus used is depicted in Figure 12. Nanofluid solution was contained in a pressure vessel downstream of the water pump. The nanoparticles were injected with the aid of nitrogen gas.

Initially, the core was preflushed with several pore volumes of pure water to displace rock fines and debris. About 30% (3 cm^3 of nanofluid) of the pore volume was then injected. Subsequent to the injection of the nanofluid, a post injection of 13 pore volumes of pure water was introduced. In addition, the core was backflushed with 5 pore volumes in attempt to mobilise nanoparticles that might be trapped at the inlet of the core. The injection was at the rate of 1 cm^3/min. A total of 40 effluent samples were collected at the rate of 2 cm^3 per sample. The effluent sample volume was increased to 6 cm^3 for the last six pore volumes. During the backflushing of the core, the flow rate was varied between 1 to 5 cm^3/min. The higher flow rates were used to investigate their effect on the mobility of the nanoparticles. SEM imaging was used to analyse the selected effluent samples.

2.9 Injection experiment results

Tin-bismuth nanoparticles were identified in a few effluent samples in very low concentrations. It was observed that only nanoparticles with diameters 200 *nm* and smaller were transported within the pore spaces of the rock, as shown in the SEM image in Figure 13A. Note that the influent sample (Figure 3) contained nanoparticles as large as 600 *nm*. It was speculated that larger particles (greater than 200 *nm*) were trapped at the inlet of the core. In fact, SEM imaging of the backflushing effluents showed that there was entrapment of various nanoparticle sizes, including the sizes greater than 200 *nm* (Figure 13B). The rock filtered the nanofluid injected allowing only a certain particle sizes to flow across it. It should be noted that this is a qualitative analysis in which the determination of the relative numbers of particles recovered was not possible.

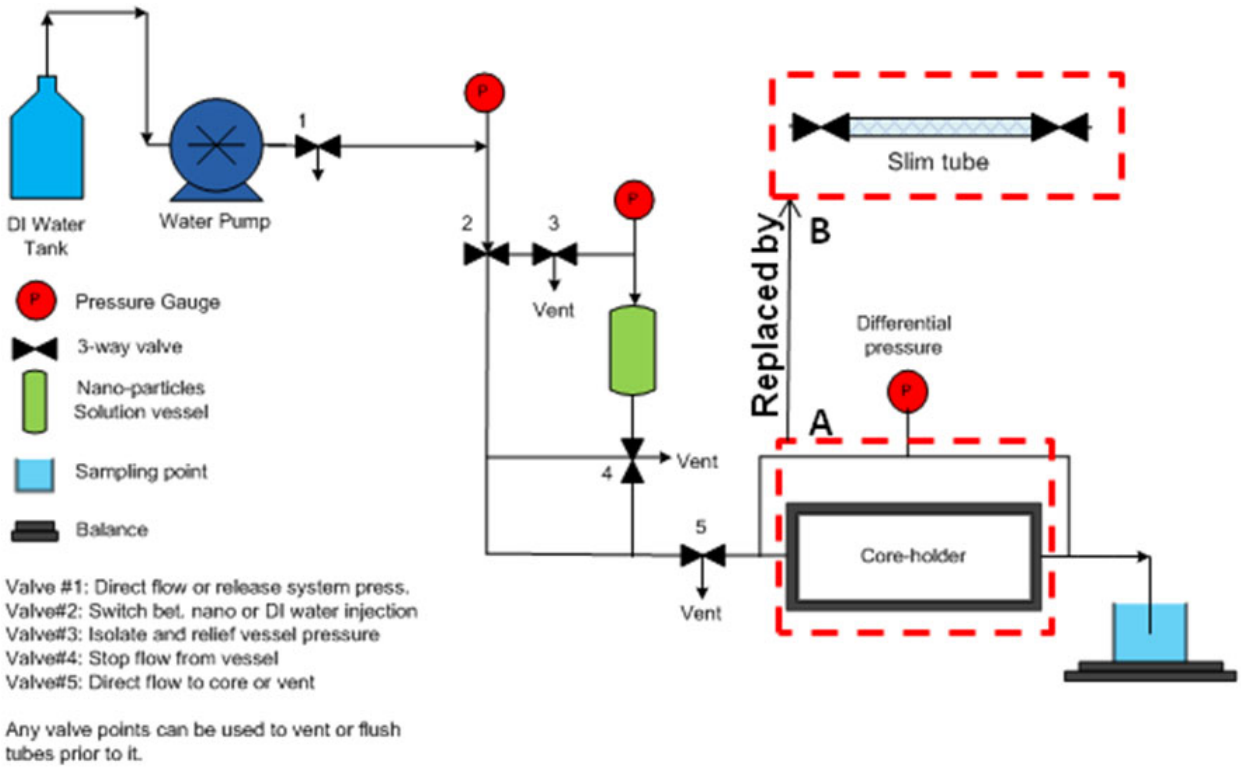

Figure 12: Schematic of the flow experiment apparatus used for injections into (A) core plug and (B) slim tube packed with glass beads.

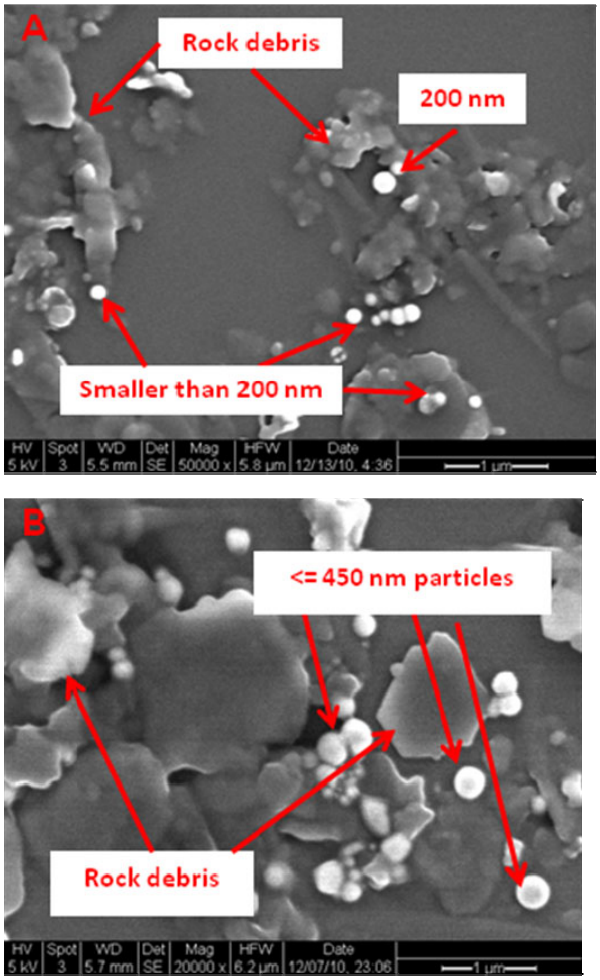

Figure 13 (left): SEM imaging showing the tin-bismuth nanoparticles at the effluent during (A) injection and (B) backflushing of the Berea sandstone. Only particles smaller than 200 nm transported through pore spaces while larger particles trapped at the inlet of the core and mobilised during backflushing.

The permeability measurements during the injection agree with this finding. The permeability as a function of the injected volume is depicted in Figure 14. There was a sudden drop in permeability to about 56% of the original value, after which the permeability remained at that level during the first post injected pore volume, indicating the partial plugging of the pores. Then, permeability started to increase until reached a plateau at approximately 82% of its value prior to the nanofluid injection. At this time, only nanoparticles of 200 *nm* and smaller were observed in the effluent, using SEM (Figure 13A). As mentioned earlier, the backflushing of the core mobilised some particles and as a result the permeability of the rock improved slightly by 8% (i.e. back to 90% of its original value).

However, permeability improvement (from 56% to 90% of original value) does not imply a good recovery of the injected nanoparticles. If the injected nanofluid has a visible color, it is possible to observe the nanoparticles in the effluent visually. In the case of the tin-bismuth injection, the influent had a dark gray color that was characterised by being highly concentrated with nanoparticles. All effluent samples appeared transparent, so it was hypothesised that many of these nanoparticles were trapped within the rock pores, most likely at

the inlet of the core. Examining the pore spaces of the rock itself confirmed that considerable numbers of the tin-bismuth nanoparticles were trapped (Figures 15 and 16).

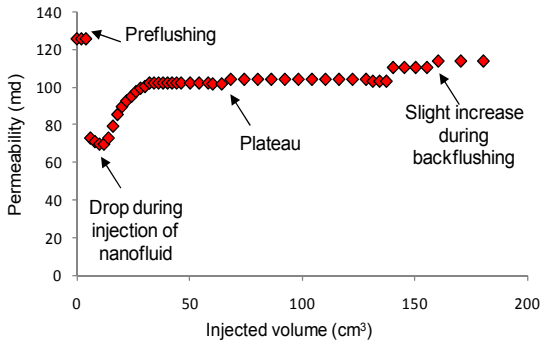

Figure 14: Permeability measurements during the injection of the tin-bismuth nanoparticles.

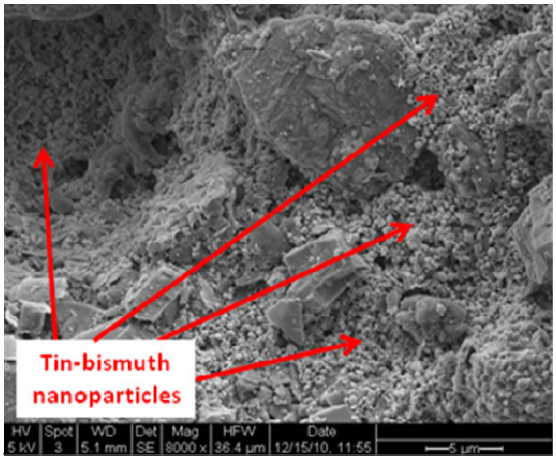

Figure 15: SEM image of the pore space at the inlet of Berea sandstone used during the tin-bismuth injection. Nanoparticle entrapment is apparent.

Further evaluation using SEM imaging (Figure 16) of the rock pore spaces demonstrates the bridging and plugging of the tin-bismuth nanoparticles in the pore throat entry. Kanj et al. (2009) explained that small particles of high concentrations might bridge across the pore throat. The authors also added that larger particles could result in direct plugging of the pore entry. Both phenomena would impact the rock permeability negatively. Particles shown in Figure 16 could not be mobilised either by increasing the injection flow rate or by backflushing and were probably responsible for the permanent reduction in the rock permeability.

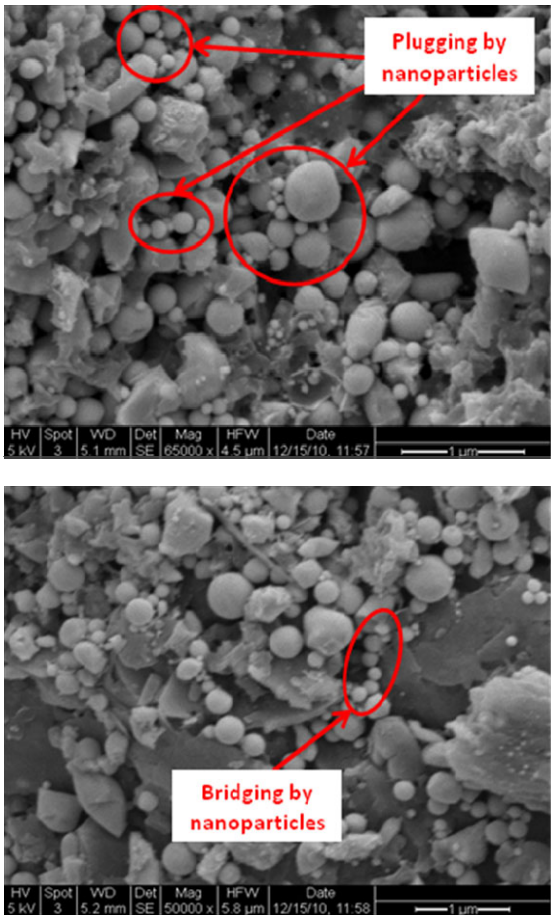

Figure 16: SEM images from within the pore spaces of the Berea sandstone. They demonstrate the bridging and plugging phenomena.

The SEM analysis did not provide conclusive evidence of the mechanism of particle entrapment. Alaskar et al. (2010) reported that the nanoparticles' shape and surface characteristics play a major role in their transport through a porous medium. They also reported that the spherical silicon dioxide (SiO_2) nanoparticles with narrow size distribution and surface charge compatible to that of the rock were transported successfully through the pore spaces of Berea sandstone. SiO_2 nanoparticles were not trapped in the pore spaces by hydraulic, chemical or electrostatic effects. The tin-bismuth nanoparticles exhibit similar properties in terms of shape and surface charge (negatively charged), except that the tin-bismuth nanoparticles had a wide distribution of sizes between 50 to 600 *nm* (Figure 2 and 3). Thus, particle shape and surface charge should not impose flow constraints. The optimised testing program suggested by Kanj et al. (2009) emphasises particle size, influent concentration and affinity of particles to rock matrix.

In the case of tin-bismuth injection, although the influent sample had wide distribution of particle sizes, they were all within the size of the pore network. Therefore, it was concluded that the tin-bismuth nanoparticles affinity and/or concentration may have caused their entrapment.

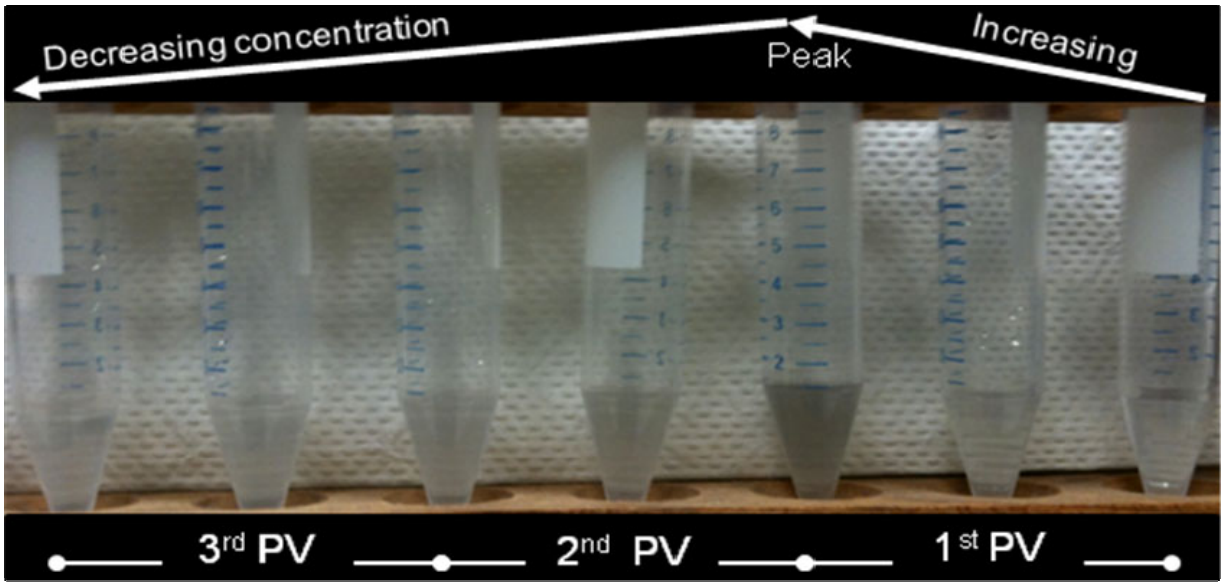

Figure 17: Visual characterisation of effluent samples for their tin-bismuth nanoparticles content based on colour.

Further investigation of particle affinity to Berea sandstone was carried out by injecting the same influent sample with identical concentration to a slim tube packed with glass beads. This allowed testing the transport of the tin-bismuth nanoparticles in the absence of the core material. One pore volume of the nanofluid was injected at the rate of 0.5 cm^3/min followed by continuous injection of pure water at the same rate. Several effluent samples were collected and analysed by SEM imaging.

It was found that the tin-bismuth nanoparticles of all sizes flowed through the slim tube. The increasing concentration of the nanoparticles was observed visually through the injection of the first post-injected pore volume as illustrated in Figure 17. SEM imaging confirmed this finding as depicted in Figure 18.

Thus, it has been demonstrated that the spherically shaped tin-bismuth nanoparticles can be recovered following their injection into tube packed with glass beads without being trapped within the flow conduits, but not through the pore network of the rock (which has much smaller pores). This might be attributed to an affinity of these nanoparticles to the sandstone rock matrix or high nanoparticle concentration imposing constraints to their flow. The complexity of the rock pore network compared the large pores in the glass beads was not taken into consideration during this analysis.

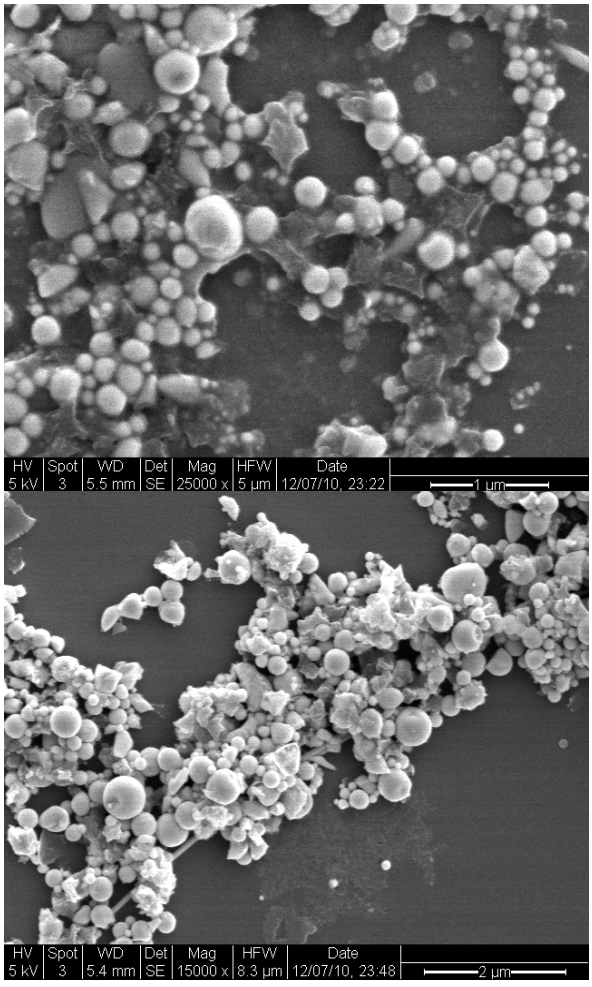

Figure 18: SEM images of the effluent collected during the injection of tin-bismuth nanoparticles into the slim tube packed with glass beads.

3. Silica nanoparticles with covalently-attached fluorescent dye

As silica particles have been proved to have transported through sandstone core successfully, we further changed their surface properties to explore their temperature response. According to the report by Wu et al. (2008), when free fluorescent dye molecule was attached to silica nanoparticles' surface, through energy transfer, the fluorescent properties of these molecules were changed. Therefore, when the covalent bond between fluorescent dye molecule and surface modified silica nanoparticle is broken under high temperature; the difference of fluorescent behavior before and after heating experiment would be detected.

3.1 Synthesis of fluorescent dye-attached silica nanoparticles

First, silica nanoparticles (Nanogiant, LLC) were prepared by surface modification. In a typical reaction, 0.5ml of 3-Aminopropyltriethoxysilane (APTS) was added to 100mg silica nanoparticle suspended in 25 ml of toluene under nitrogen and heating to ~95 °C for 4 hours. The resulting particles were washed by centrifugation in ethanol and acetone (10min at 4,400 rpm). Then the particles were dried at ~95°C overnight.

After that, we attached dye molecules (Oregon 488, Invitrogen) to the surface of the modified silica nanoparticles. A suspension of 1.0 mg of the amino-modified Silica nanoparticles in a mixture of 1ml of ethanol and 15 μl of a 10mmol/L phosphate buffer (pH 7.3) was reacted with 12.7 μl of dye molecule solution (1mg/ml water solution) in dark for 3 hours at room temperature. The resulting particles were washed by centrifugation (10min at 4,400 rpm) in ethanol and acetone.

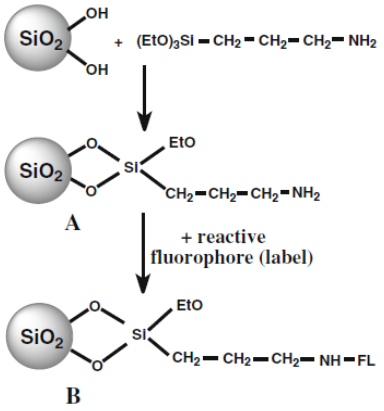

Figure 19: Schematic representation of silica nanoparticle surface modification and dye attachment by Saleh, et al. (2010).

We also performed surface modification and dye attachment reaction on a monolayer of silica nanoparticles on quartz substrate using the same experiment parameters.

3.2 Characterisation of silica nanoparticles

We used Fluorescent Microscopy, SEM and Fluorescent Spectrum to characterise the dye-attached silica nanoparticles.

Fluorescent microscopy characterisation as shown in Figure 20 was done using the substrate base dye-attached silica nanoparticle sample. We can see clearly that the dye molecules were attached successfully to the surface of silica nanoparticles. The whole substrate was fluorescent although not uniformly (some spots were brighter with more fluorescent molecules attached).

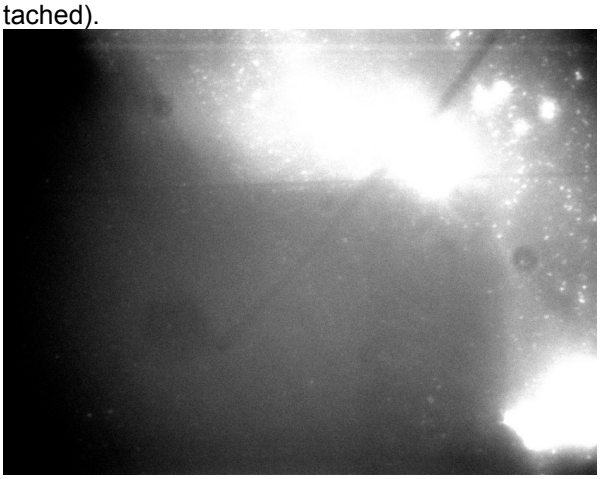

Figure 20: Fluorescent microscopy image of dye-attached silica nanoparticles on quartz substrate.

SEM was also used for characterisation.

We also measured the fluorescence spectra of free dye molecule solution, silica nanoparticle suspension, dye-attached silica nanoparticles both on substrate and in solution.

We used 400nm as the excitation wave length. We could see from the fluorescence spectrum of Oregon 488 solution that its emission peak is at ~530nm, shown in Figure 21.

As control, we measured the fluorescence spectrum of silica nanoparticles in water without dye attachment. We also measured the fluorescence spectra of dye-attached silica nanoparticles in water and on substrate. We used 400nm as excitation wavelength, shown in Figure 22. The results showed that, without dye attachment, there was no fluorescence response of the silica nanoparticles and after dye attachment, two peaks at ~425nm and ~530nm were observed in the spectrum.

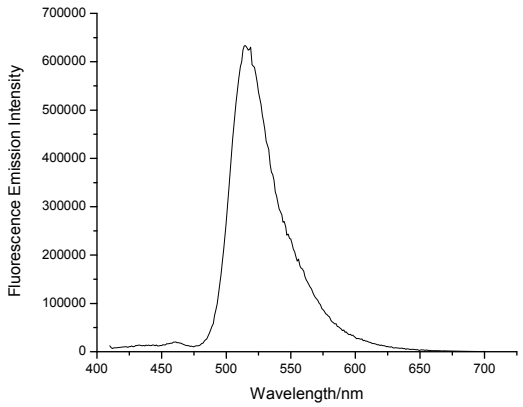

Figure 21: Fluorescence spectrum of Oregon 488 dye molecule solution (excitation wavelength 400nm).

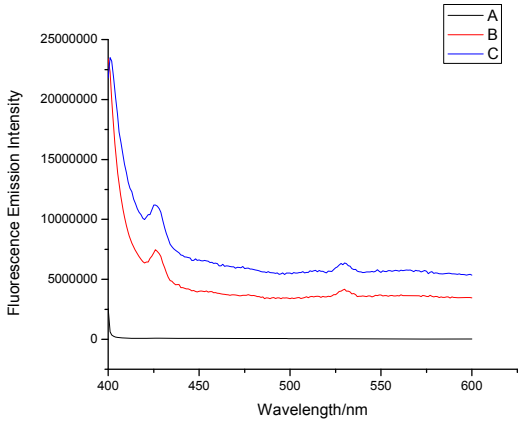

Figure 22: Fluorescence spectrum (excitation wavelength 400nm): (A) Silica nanoparticle without dye attachment as control; (B) Dye-attached silica nanoparticles in water; (C) Dye-attached silica nanoparticles on quartz substrate.

3.4 Heating experiment of dye-attached silica nanoparticle

A heating experiment was conducted using the sample of dye-attached silica nanoparticles on quartz substrate. We heated the substrate on a hot plate at 200°C for 15min. Then we soaked the substrate in ethanol and acetone respectively and washed the substrate both with ethanol and acetone. The substrate was dried in air. We used Fluorescence Spectrum to characterise this sample.

Fluorescence spectrum was measured after heating test, shown in Figure 23. We used an excitation wavelength of ~360nm. We can observe a wide peak at ~425nm of the heated sample which was obviously different from the sample before heating. Besides that, we observed at ~380nm and ~475nm there were two shoulder peaks and at ~575nm there was a small peak in both spectra.

Hence, a clearly identifiable property change (fluorescence) is available as a temperature indicator using this kind of nanoparticle.

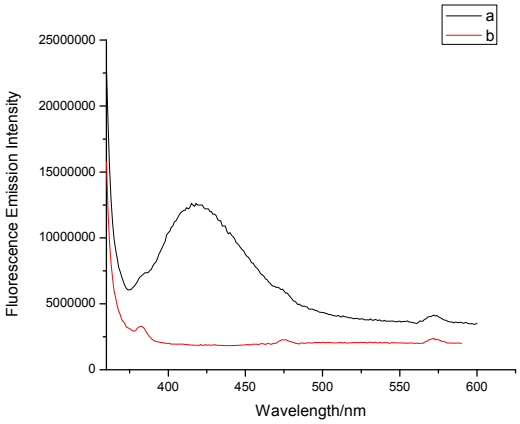

Figure 23: Fluorescence spectrum (excitation wavelength 360nm): (a) Dye-attached silica nanoparticle after heating experiment at 200°C for 15min; (b) Dye-attached silica nanoparticle without heating experiment.

4. Estimating the location of temperature measurements using dye-release nanosensors

We have demonstrated the potential capability of dye-attached silica nanoparticles to measure temperature in geothermal reservoirs. However, simply knowing that some region of the reservoir has a certain temperature without knowing the geolocation of the measurement is of limited use to reservoir engineers. If this geolocation could be estimated accurately, the reservoir temperature distribution could be mapped. This could make it possible to predict thermal breakthrough in a reservoir and would allow reservoir engineers to make more informed decisions. Here we discuss the potential capability of a nanosensor with a dye-release sensing mechanism (e.g. dye-attached silica nanoparticles) to measure reservoir temperature and estimate the geolocation of this measurement via analysis of the return curve of the released dye.

A thought experiment was performed consisting of two hypothetical tracer tests: one with a conservative solute tracer and one with dye-releasing nanosensors. Synthetic tracer return curves for these hypothetical tests were generated using an analytical solution to the advection-dispersion equation, which is often used to describe subsurface tracer flow. Juliusson and Horne (2011) expressed the one-dimensional form of this equation as:

$$R\frac{\partial C}{\partial t} = \alpha u \frac{\partial^2 C}{\partial x^2} - u\frac{\partial C}{\partial x} \qquad (1)$$

where C is tracer concentration, x is the spatial coordinate, t is time, u is the flux velocity, and α is

the dispersion length, and *R* is the tracer retardation factor, which accounts for the retardation of tracer transport caused by the reversible adsorption of tracer to rock interfaces. For this initial investigation, the simple case with a constant flux velocity *v* (i.e. constant flow rate) was considered, and it was assumed that *R* is constant with respect to *t*, *x*, and *C* for both the solute tracer and the nanosensors. The authors acknowledge that it might be more realistic to assume that *R* varies spatially, as is suggested by Chrysikopoulos (1993), and that nanoparticle flow likely requires even more complex treatment. With these caveats in mind, it was decided to first examine the simplest possible case.

Kreft and Zuber (1978) provided a solution to the advection-dispersion equation with flux injection and detection boundary conditions, and Juliusson and Horne (2011) rewrote this solution to include the retardation factor *R*:

$$C = \frac{mV_x}{qt\sqrt{4\pi V_\alpha qt}} \exp\left(-\frac{\left(qt - V_x\right)^2}{4V_\alpha qt}\right) \quad (2)$$

$$V_x = RA\phi x \quad (3)$$

$$V_\alpha = RA\phi\alpha \quad (4)$$

where *m* is the mass injected, *q* is the volumetric flowrate, *t* is time, V_x is the pore volume modified by the retardation factor *R*, V_α is the dispersion volume modified by *R*, *A* is cross-sectional area, φ is porosity, and α is the dispersion length.

Consider a geothermal reservoir that consists of a single fracture with length *L*, cross-sectional area *A*, and porosity φ. Before exploitation, the reservoir had a uniform temperature distribution with a temperature of T_1. Some years after the onset of exploitation, the thermal front has advanced to the position x_f, and the portion of the reservoir behind the front has cooled to temperature T_2, as shown in Figure 24. Suppose a nanosensor has been designed to release a fluorescent dye at the threshold temperature T_1, and assume that this release occurs instantaneously upon exposure to this threshold.

Two tracer tests are performed. In one test, a mass m_c of a conservative tracer with a retardation factor R_c is injected into the reservoir. The tracer is sampled at the production well (i.e. *x* = *L*), and the return curve can be described by Equations 5 – 7:

$$C_c = \frac{m_c V_{x,c}}{qt\sqrt{4\pi V_{\alpha,c} qt}} \exp\left(-\frac{\left(qt - V_{x,c}\right)^2}{4V_{\alpha,c} qt}\right) \quad (5)$$

$$V_{x,c} = R_c A\phi L \quad (6)$$

$$V_{\alpha,c} = R_c A\phi\alpha \quad (7)$$

where the subscript *c* denotes the conservative tracer.

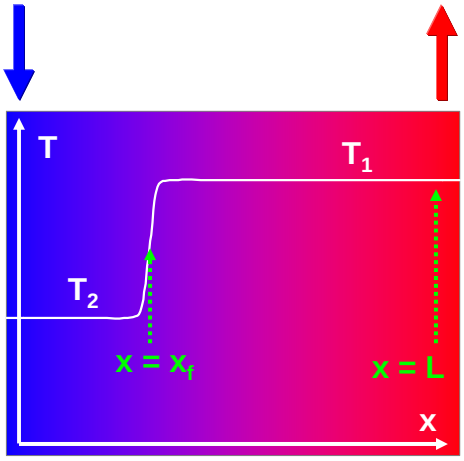

Figure 24: Cartoon of temperature distribution in a geothermal reservoir with a thermal front at position x_f .

In the second test, a slug of the dye-releasing nanosensors with retardation factor R_n is injected into the reservoir. Upon reaching exposure to the threshold temperature T_2 at position x_f, the nanosensors release a mass m_r of the attached dye, which itself behaves like the conservative solute tracer in the previous tracer test, and has a retardation factor R_c. The released dye is sampled at the production well. The return curve of the released dye is influenced by both R_n and R_c, because it travels with the nanosensor retardation factor R_n from *x = 0* to *x* = x_f and the retardation factor R_c from *x* = x_f to *x* = *L*. Thus, the return curve of the released dye can be described by Equations 8 – 11:

$$C_r = \int_0^t \frac{m_r V_{x,n}}{qt\sqrt{4\pi V_{\alpha,n} q(t-\tau)}} \exp\left(-\frac{\left(q(t-\tau) - V_{x,n}\right)^2}{4V_{\alpha,n} q(t-\tau)}\right) \bullet \frac{qV_{x,r}}{qt\sqrt{4\pi V_{\alpha,c} q\tau}}$$

(8)

$$V_{x,n} = R_n A\phi x_f \quad (9)$$

$$V_{\alpha,n} = R_n A\phi\alpha \quad (10)$$

$$V_{x,r} = R_c A\phi\left(L - x_f\right) \quad (11)$$

where the subscript *n* denotes the nanosensors and the subscript *r* denotes the released dye. Note that $V_{x,r}$ can be rewritten as:

$$V_{x,r} = V_{x,c} - \frac{V_{\alpha,c}}{V_{\alpha,n}} V_{x,n} \quad (12)$$

Thus, the return curves for the conservative tracer can be fit to Equation 5 by adjusting the values of unknowns $V_{x,c}$ and $V_{\alpha,c}$ (i.e. minimising the norm of the differences between the return curve data and the model with the unknowns as decision

variables). Subsequently, the return curves for the released dye can be fit to Equation 8 by adjusting the values unknowns $V_{x,n}$ and $V_{\alpha,n}$. Note that $V_{x,r}$ is not explicitly adjusted here because it can be expressed in terms of the other unknowns. Once the values of the unknowns have been determined, one can calculate the geolocation of the thermal front using Equation 13:

$$x_{f,d} = \frac{x_f}{L} = \frac{V_{x,c} - V_{x,r}}{V_{x,c}} \qquad (13)$$

where $x_{f,d}$ is the dimensionless position of the thermal front.

This analysis was demonstrated successfully in an example problem with the parameter values shown in Table 1.

Table 1: Parameter Values Used In Return Curve Analysis Demonstration Problem

Parameter	Value
R_c	2
R_n	1
A	200 m^2
φ	0.10
L	1000 m
α	25 m
Pe = L / α	40

These values were chosen somewhat arbitrarily for the purposes of this demonstration. However, values of R_c and R_n were used such that the nanosensors experience no retardation and the solute tracer does experience retardation. This is based on studies of colloid transport in fractures which showed that colloids exhibit breakthrough more rapidly than solute tracers because they tend to stay in fluid streamlines and do not experience matrix diffusion (Reimus 1995).

Synthetic return curve data for the conservative tracer and the nanosensors were generated for various values of x_f using Equations 5 and 8, and Gaussian noise was added for the sake of realism. An optimisation solver was then used to find the best fit to Equations 5 and 8 by adjusting the unknowns. The results are tabulated in Table 2, and select return curves are plotted in Figure 25.

Reasonably good estimates of the geolocation of the thermal front were obtained for all scenarios except for x_f = 0.05. This is physically intuitive, because the return curves for the conservative tracer and the released dye are almost identical when the thermal front is still close to the injection well, making it difficult to estimate the front geolocation quantitatively. The poor fit of the return curve of the released dye can be attributed mathematically to the problematic nature of the optimisation surface for this scenario, which is shown in Figures 26 and 27.

Table 2: Parameter Values Used In Return Curve Analysis Demonstration Problem

$x_{f,d}$	$x_{f,d}$ estimate	Error
0.05	0.037	26%
0.15	0.155	3.2%
0.25	0.248	0.8%
0.35	0.382	9.1%
0.45	0.431	4.3%
0.55	0.517	5.9%
0.65	0.632	2.7%
0.75	0.746	0.6%
0.85	0.852	0.2%
0.95	0.925	2.7%

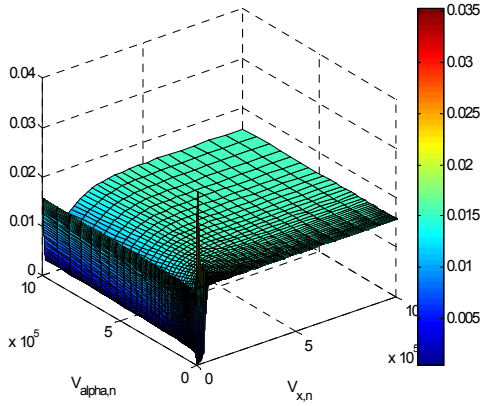

Figure 26: Objective function surface for fitting the return curve of the reactive tracer when x_f = 50 m.

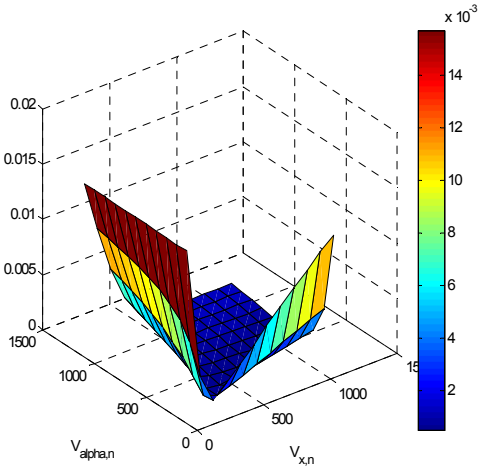

Figure 27: Objective function surface for fitting the return curve of the reactive tracer when x_f = 50 m, zoomed in near the minimum of ($V_{x,n}$ = 1000 m^3, $V_{\alpha,n}$ = 500 m^3). Note that the point chosen by the solver was ($V_{x,n}$ = 268.3 m^3, $V_{\alpha,n}$ = 180.8 m^3).

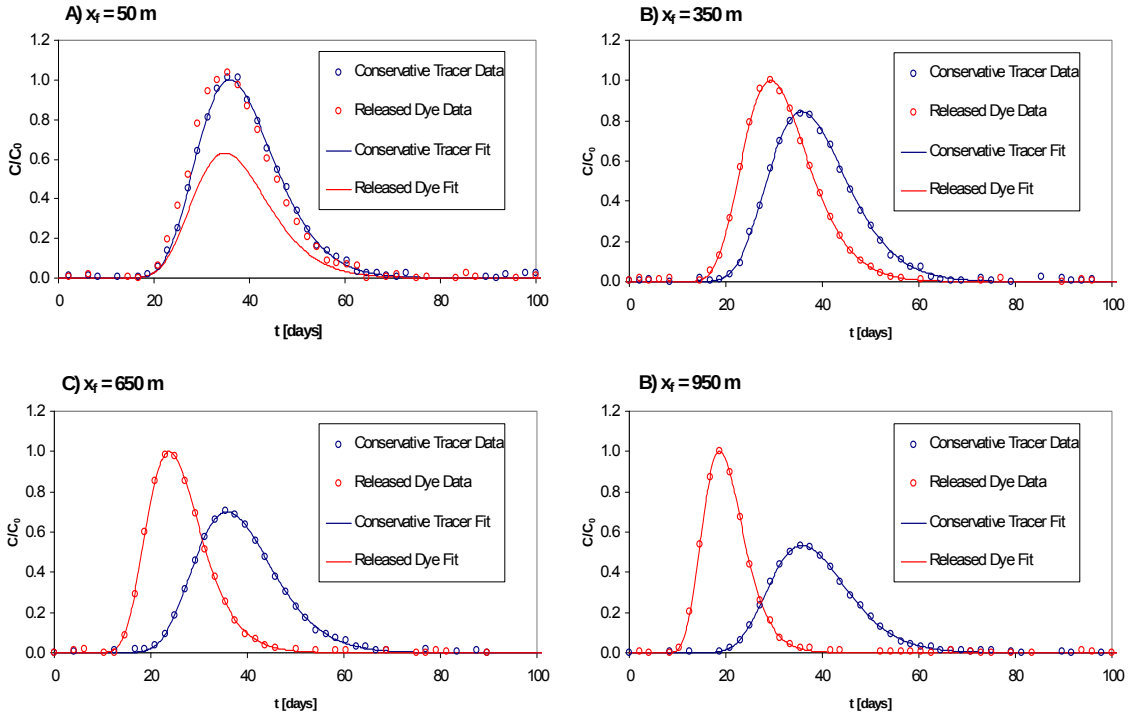

Figure 25: Return curve data and fits for A) x_f = 50 m, B) x_f = 350 m, C) x_f = 650 m, and D) x_f = 950 m. Note that released dye experiences breakthrough first because it is carried a distance x_f by the nanosensor, which has a retardation factor of 1, while the conservative tracer has a retardation factor of 2.

The large trough along the $V_{\alpha,n}$ axis in Figure 26 indicates that for large initial guesses of $V_{\alpha,n}$, the solver might get stuck far from the minimum (since change in the objective function is the termination criteria). Moreover, the values of the objective function vary very little near the minimum, as shown in Figure 27. This explains why the solver terminated at the point ($V_{x,n}$ = 268.3 m^3, $V_{\alpha,n}$ = 180.8 m^3) and resulted in a poor fit.

5. Conclusions

We have synthesised two types of temperature-sensitive nanoparticles and demonstrated their sensitivity in the geothermal temperature range. The two types are melting tin-bismuth alloy nanoparticles and silica nanoparticles with dyes incorporated using a temperature-sensitive covalent linkage. We performed an initial investigation of the feasibility of estimating the geolocation of temperature measurements using return curve analysis for a dye-releasing nanosensor.

Tin-bismuth alloy nanoparticles were synthesised using a sonochemical method. A heating experiment was performed using these nanoparticles, and particle growth was observed, which was indicative of melting. The flow characteristics of the tin-bismuth nanoparticles were also investigated. Tin-bismuth nanoparticles of all sizes were transported successfully through the slim-tube. However, when nanoparticles were injected into a Berea sandstone core, only particles with diameters of 200 *nm* and smaller were detected at very low concentrations in the effluent. Nanoparticle plugging and bridging was detected at the core inlet. As measurements of the particle size and surface charge did not indicate any flow constraints, entrapment was attributed either to an affinity of the tin-bismuth to the sandstone rock matrix or an excessively high nanoparticle concentration at the inlet, or both.

Moreover, dye-attached silica nanoparticles were synthesised through surface modification and fluorescent reaction. We demonstrated the successful synthesis by SEM and fluorescence spectrum characterisation. A heating experiment was also conducted using a sample of silica nanoparticles on substrate. The results showed that the fluorescence spectra of dye-attached silica nanoparticles in water and on quartz substrate are the same. After heating, the fluorescence spectrum showed an obvious difference at a wavelength of 425nm. Although the mechanism of this phenomenon is not fully understood yet, we did discover the excellent potential of dye-attached silica nanoparticles as temperature sensors for geothermal applications.

To emphasise the potential usefulness of a nanosensor with a dye-release mechanism (such as dye-attached silica nanoparticles), an initial study was performed to evaluate the feasibility of estimating the geolocation of temperature measurements by analysing the return curve of the released dye. Accurate estimation of measurement

geolocations would allow one to map the temperature distribution in a geothermal reservoir and provide information about thermal breakthrough. A simplified example problem was examined in which an analytical solution of the one-dimensional advection-dispersion equation was used to generate synthetic return curve data for two tracer tests: one with a conservative tracer and one with dye-releasing nanosensors. Gaussian noise was added to the synthetic data. Finally, return curves were fit to the data by adjusting the values of four unknowns (two unknowns for each return curve). Reasonably accurate estimates of the measurement geolocation were achieved for various scenarios, with the exception of a poor estimate when the thermal front had not advanced very far into the reservoir. This could possibly be remedied by using a more sophisticated optimisation algorithm.

6. Acknowledgements

The authors wish to thank Robert Jones, Sirion SEM Laboratory Manager, for his support during this project. The authors also acknowledge the continued support of the Department of Energy (under contract number DE-FG36-08GO18192).

7. References

Alaskar, M., Ames, M., Horne, R.N., Li, K., Connor, S. and Cui, Y.: "In-situ Multifuction Nanosensors for Fractured Reservoir Characterisation," GRC Annual Meeting, Sacramento, USA, vol. 34 (2010).

Botterhuis, N., Sun, Q., Magusin, P., Santen, R. and Sommerdijk, N.: "Hollow Silica Spheres with an Ordered Pore Structure and Their Application in Controlled Release Studies," *Chem. Eur. J.* 2006, **12**, 1448-56.

Chen, H., Li, Z., Wu, Z. and Zhang, Z.: "A novel route to prepare and characterize Sn-Bi nanoparticles," *Journal of Alloys and Compounds*. 2005, **394**, 282-285.

Digital image. Phase Diagrams & Computational Thermodynamics. The National Institute of Standards and Technology. Web. 7 July 2010. <http://www.metallurgy.nist.gov/phase/solder/bisn.html>.

Juliusson, E., and Horne, R.N.: "Analyzing Tracer Tests During Variable Flow Rate Injection and Production," Proc. of Thirty-Sixth Workshop on Geothermal Reservoir Engineering, Stanford University, Stanford, CA. 2011.

Kanj, M., Funk, J., and Al-Yousif, Z.: "Nanofluid Coreflood Experiments in the Arab-D," SPE paper 126161, presented at the 2009 SPE Saudi Arabia Technical Symposium and Exhibition held in Saudi Arabia, Alkhobar, May 09-11.

Kreft, A. and Zuber, A..: "On the physical meaning of the dispersion equation and its solutions for different initial and boundary conditions," *Chemical Engineering Science*. 1978, **33**(11), 1471–1480.

Reich, M., Utsunomiya, S., Kesler, S.E., Wang, L., Ewing, R.C., and Becker, U.: "Thermal behavior of metal nanoparticles in geologic materials," Geol. Soc. Am. **34**(2006).

Saleh, S.M., Muller, R., Mader, H.S., Duerkop, A., Wolfbeis, O.S.: "Novel multicolor fluorescently labeled silica nanoparticles for interface fluorescence resonance energy transfer to and from labeled avidin," *Anal Bioanal Chem* (2010) 398:1615-1623.

Sing, C., Kunzelman, J., and Weder, C.: "Time-temperature indicators for high temperature applications," *J. Mater. Chem.* **19** (2009).

Wu, E.C., Park, J.H., Park, J., Segal, E., Cunin, F., and Sailor, M.J.: Oxidation-triggered release of fluorescent molecules or drugs form mesoporous Si Microparticles," *ACS Nano* (2008), Vol.2 No.11:2401-2409.